proceedings

Non-destructive testing of CFRP DCB specimens using active thermography †

Ding-En Wu [1],*, Chih-Hung Chiang [2],* ,Mahesh [3], Keng-Tsang Hsu [4]

[1] Department of Civil and Construction Engineering, Chaoyang University of Technology, Taichung City 413310, Taiwan; s11211602@gm.cyut.edu.tw
[2] Center for NDT and Graduate Institute of Aeronautics, Chaoyang University of Technology, Taichung City 413310, Taiwan; chiangc@cyut.edu.tw
[3] Graduate Institute of Aeronautics, Chaoyang University of Technology, Taichung City 413310, Taiwan; t2024016@gm.cyut.edu.tw
[4] Department of Civil and Construction Engineering, Chaoyang University of Technology, Taichung City 413310, Taiwan; frankhsu@cyut.edu.tw
* Correspondence: s11211602@gm.cyut.edu.tw; chiangc@cyut.edu.tw
† Presented at the "Advanced Infrared Technology and Application (AITA)" in Kobe, Japan, on 15-19 September 2025

Mode I Interlaminar Fracture Toughness test of carbon fiber reinforced polymer laminates requires a double cantilever beam (DCB) specimen with a pre-implanted non-adhesive insert at the mid-plane to initiate delamination. However, the insert's quality and placement within the DCB specimen can be problematic, necessitating non-destructive testing methods. In this study, active thermography is employed to inspect potential defects around the Teflon insert in the DCB specimens. Both uniform and non-uniform heating methods have been applied, and thermal images was analyzed to obtain quantitative information, such as the insert's location and non-contact area. TSR-enhanced images were obtained using two variations of the classical thermographic signal reconstruction. The analyzed results confirmed the presence of non-contact areas in the DCB structures composed of both 22-layer and 24-layer CFRP prepregs. These areas may be attributed to residual air gaps formed during the hot-press molding of the DCB structures.

Keywords: carbon fiber reinforced composite; active thermography; double cantilever beam specimen;

Citation: To be added by editorial staff during production.

Academic Editor: Firstname Lastname

Published: date

1. Research Motivation

Carbon fiber reinforced polymer (CFRP) composites are prone to interlaminar cracking in structural applications [1]. As such, investigating their interlaminar fracture toughness is critical for the development and selection of composite structure designs. To facilitate subsequent fracture toughness testing, Double Cantilever Beam (DCB) specimens with three different stacking sequences were fabricated, incorporating a non-adhesive film at the mid-plane on one side to initiate delamination [2, 3]. To assess the integrity of the specimens, active infrared thermography [4] was employed to examine potential unbonded regions between the inserted film and the adjacent CFRP prepreg layers.

2. Infrared Thermography Experimental Method

Standard CFRP DCB coupon specimens are typically prepared from large test pieces fabricated using unidirectional carbon fiber (0.1mm thick) prepregs. We will refer to the test piece as the specimen hereafter. The specimens, measuring 160 mm long, 135 mm wide, and 2.1 mm thick, were created in 22, 24, and 26-layer configurations. To pre-induce cracks, a 0.03 mm thick layer of Teflon was inserted in the middle of each specimen. All specimens were hot-pressed at 40 kgf/cm² to achieve a final thickness of 2.1

mm.

On the back side of each completed CFRP specimen, two 500 W halogen lamps were used as the thermal excitation source. Infrared imaging was performed on the front side using an AVIO R500 thermal camera, with data recorded over a 20-second heating period at a frame rate of 3 Hz.

3.Thermal Image Analysis

After data extraction, relative temperature differences were calculated by subtracting the initial frame (baseline temperature) from each subsequent thermal image. These temperature differences were then analyzed as a function of time, and fitted using polynomial models of degree deg. In addition to direct time-temperature analysis, logarithmic transformations (lnt and ΔlnT)were also employed to construct polynomial fittings (Equations 1 and 2). Polynomial degrees of 3 and 5 were adopted, resulting in a total of four different processing approaches.

$$\Delta T(t)=a_0+a_1 t+a_2 t^2+a_3 t^3+\cdots+a_{deg} t^{deg} \quad (1)$$

$$\Delta ln(T)=a_0+a_1 ln(t)+a_2 ln(t)^2+a_3 ln(t)^3+\cdots+a_{deg} ln(t)^{deg} \quad (2)$$

In order to improve signal clarity, the natural logarithm of temperature and time data was taken and then subtracted. This is equivalent to dividing the original data and it was done to avoid errors that can occur when polynomial fitting is applied to temperature difference data, especially when it contains zeros or negative numbers. The polynomial-fitted data was further processed by applying non-derivative, first-order, and second-order derivatives to create enhanced images. The clearest image showing the defect was selected for analysis. Temperature differences were categorized using a normal distribution model, dividing the thermal data into high-temperature (specimen background) and low-temperature regions (defects and aluminum foil).

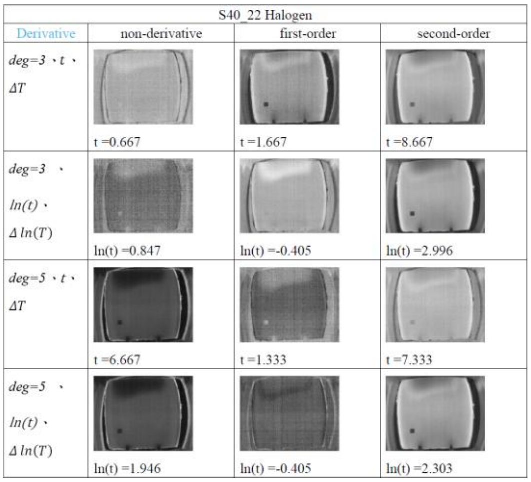

Figure 1. S40-22 Enhanced image

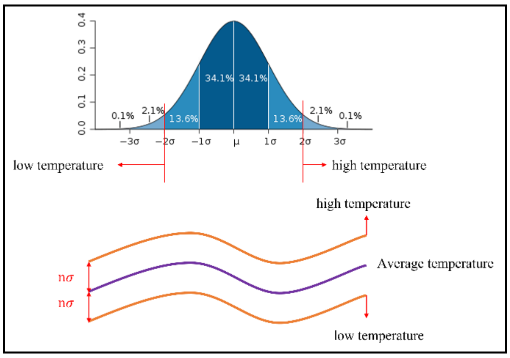

Figure 2. Normal distribution diagram

An analysis region was first defined within the thermal images, with its size set to be at least n times larger than the target area to be evaluated—for example, 6~8 times larger for the aluminum foil and 3~4 times larger for defect areas, as this yielded more stable results (Figure 3). A normal distribution analysis was then applied to this region. The number of low-temperature pixels was determined using a threshold defined as the mean temperature minus n times the standard deviation. Three classification criteria were used:

(1) pixels with temperature differences lower than the average (Avg),

(2) lower than the average minus one standard deviation (Avg − σ, or SD), and
(3) lower than the average minus two standard deviations (Avg − 2σ, or SD2).

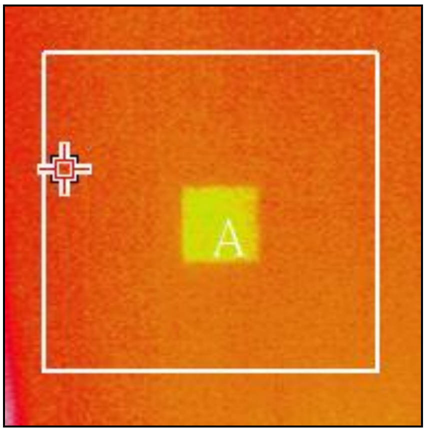

Figure 3. The white box is the aluminum paper data, about 6 to 8 times the size of the aluminum foil

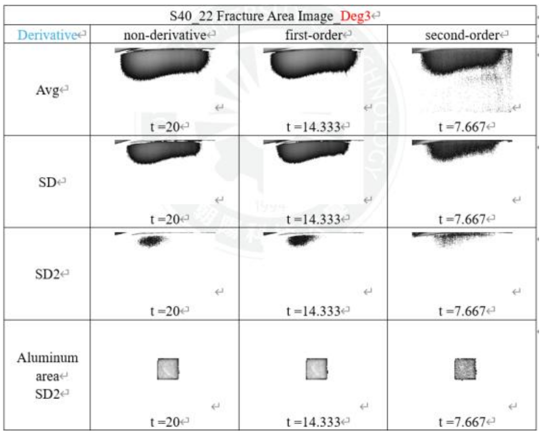

Figure 4. S40-22 Deg3 Defect enhanced grayscale images

4. Results and Discussions

The low-temperature pixel regions were retained and visualized as binary images (Figure 4, showing S40-22 Deg3 as an example) to facilitate comparison. Since the number of aluminum foil pixels under the non-derivative condition using the Avg − 2σ (SD2) criterion closely corresponded to 1 cm²—the actual area of the foil—we adopted the SD2 threshold for aluminum foil area estimation. Subsequently, we identified the frame in the first- and second-order derivative results where the aluminum foil pixel count matched or closely approximated that of the non-derivative SD2 case. This frame was then used for further defect area analysis.

As shown in Figure 4, both potential defective and foil regions were compared. However, it was observed that in the second-order derivative condition, the aluminum foil pixel count significantly deviated from that of the non-derivative SD2 reference, and the defect region exhibited considerable noise. Therefore, results from the second-order derivative condition were excluded from further analysis.

In the TSR-enhanced images, a suspected rectangular-shaped defect was observed in the 22-ply specimen, while a triangular-shaped suspected defect appeared in the 24-ply specimen. No distinct temperature anomalies were detected in the 26-ply specimen. For defect area estimation, the aluminum foil pixel count was consistently determined using the Avg − 2σ (SD2) criterion, and the corresponding defect pixel count was taken from the same frame. Additionally, several temperature profiles were drawn to extract the vertical and horizontal dimensions of the suspected defect regions using the Full Width at Half Maximum (FWHM) method.

For the 22- and 26-ply specimens, the upper and lower bounds of the defect area were estimated by multiplying the vertical and horizontal lengths. In contrast, the 24-ply specimen's suspected defect area was calculated using the triangle area formula due to its shape. The estimated defect area ranges for each specimen, based on four different processing approaches—including polynomial fitting and logarithmic transformations—are summarized in Tables 1 through 3.

Table 1. Estimated Defect Area Range (cm^2) for S40-22 under Different Polynomial and Statistical Methods

method	Deg3	Deg3ln	Deg5	Deg5ln
Avg	42.2~44.7	40.9~44.4	41.2~45	42~44.6
SD	25.5~26.2	24.8~26.6	26~26.6	26~26.2

SD2	4.3~5.5	4~6.1	3.8~5.5	4.6~5.3

Table 2. Estimated Defect Area Range (cm²) for S40-24 under Different Polynomial and Statistical Methods

method	Deg3	Deg3ln	Deg5	Deg5ln
Avg	54.2~54.4	53.4~54.4	53.9~54.4	53.8~54.2
SD	33.3~35.9	33.6~35	33.5~36.4	33.2~36.1
SD2	4.8~7.8	6~8	4~7.2	5~8.5

Table 3. Estimated Defect Area Range (cm²) for S40-26 under Different Polynomial and Statistical Methods

method	Deg3	Deg3ln	Deg5	Deg5ln
Avg	55.8~57.8	55.2~56.9	55.9~57.1	55.5~57.6
SD	23.7~24.8	23.8~24.9	23.9~24.4	23.5~24.6
SD2	1.6~1.8	1.5~1.8	1.8~2	1.7~1.8

Table 4. Defect Area Estimates (cm²) Selected by FWHM Analysis and Defect-to-Aluminum Statistical Threshold Ratios

	S40-22	S40-24	S40-26
Calculation Method	Defect SD / Aluminum SD2	Defect SD / Aluminum SD2	Defect Avg / Aluminum SD2
Area(〖cm〗^2)	24.8~26.6	33.2~36.4	55.2~57.8

In particular, the selected pixel count within the region of interest for the 26-ply specimen was based on the average temperature (Avg) criterion (Table 3). This adjustment was made because the temperature difference between the low-temperature region and the surrounding area in the 26-ply specimen was relatively small (less than 1°C), compared to over 2°C in the other two specimens. As a result, the FWHM method yielded a broader width for the low-temperature region, leading to an overly large estimation of defect area, as shown in Table 4.

Author Contributions: Conceptualization and methodology: D.W. and C.C.; software, validation, formal analysis, data curation, and investigation: D.W. and M.; Writing—original draft preparation, D.W.; writing—review and editing: C.C. and K.H.; project administration, and funding acquisition: C.C.

Funding: This work was supported by NSTC, Taiwan. Project number NSTC 113-2221-E-324-005.

Conflicts of Interest: The authors declare there are no conflicts of interest.

References

1. He, H.H. Thermographic inspection and thermal analysis of an experimental wind turbine blade. Master's thesis, Chaoyang University of Technology, Taichung, Taiwan, 2013.
2. ASTM D5528/D5528M–21: Standard Test Method for Mode I Interlaminar Fracture Toughness of Unidirectional Fiber-Reinforced Polymer Matrix Composites. ASTM International: West Conshohocken, PA, USA, 2021.
3. Reiner, J.; Chen, C; Vaziri, V.; Poursartip, A; Combining digital image correlation and phased-array ultrasonics for non-destructive testing of translaminar fracture in composite laminates. *Composites Part A: Applied Science and Manufacturing*, 2022, 161, 3-11.
4. Huang, Z; Zhu, J.; Zhuo, L.; Li, C; Liu, C; Hao, W; Xie, W. Non-destructive evaluation of uneven coating thickness based on active long pulse thermography. *NDT and E International*, 2022, 130, 3-6.